Published in final edited form as:
IEEE Trans Comput Imaging. 2020 ; 6: 1375–1388. doi:10.1109/tci.2020.3023598.

Contrast-Medium Anisotropy-Aware Tensor Total Variation Model for Robust Cerebral Perfusion CT Reconstruction with Low-Dose Scans

Yuanke Zhang,
School of Biomedical Engineering, Southern Medical University, Guangzhou 510515, China, and also with the School of Information Science and Engineering, Qufu Normal University, Rizhao 276826, China

Jiangjun Peng,
School of Mathematics and Statistics, Xi'an Jiaotong University, Xi'an 710049, China

Dong Zeng,
School of Biomedical Engineering, Southern Medical University, Guangzhou 510515, China

Qi Xie,
School of Mathematics and Statistics, Xi'an Jiaotong University, Xi'an 710049, China

Sui Li,
School of Biomedical Engineering, Southern Medical University, Guangzhou 510515, China

Zhaoying Bian,
School of Biomedical Engineering, Southern Medical University, Guangzhou 510515, China

Yongbo Wang,
School of Biomedical Engineering, Southern Medical University, Guangzhou 510515, China

Yong Zhang,
School of Mathematics and Statistics, Xi'an Jiaotong University, Xi'an 710049, China

Qian Zhao,
School of Mathematics and Statistics, Xi'an Jiaotong University, Xi'an 710049, China

Hao Zhang,
Department of Radiation Oncology, Stanford University, Stanford, CA 94305, USA

Zhengrong Liang,
Departments of Radiology and Biomedical Engineering, State University of New York at Stony Brook, NY 11794, USA

Hongbing Lu,
School of Biomedical Engineering, Fourth Military Medical University, Xi'an 710032, China

Deyu Meng,
School of Mathematics and Statistics, Xi'an Jiaotong University, Xi'an 710049, China

---

(*Corresponding author: Deyu Meng; Jianhua Ma*. dymeng@mail.xjtu.edu.cn, jhma@smu.edu.cn).

Jianhua Ma
School of Biomedical Engineering, Southern Medical University, Guangzhou 510515, China

Abstract

Perfusion computed tomography (PCT) is critical in detecting cerebral ischemic lesions. PCT examination with low-dose scans can effectively reduce radiation exposure to patients at the cost of degraded images with severe noise and artifacts. Tensor total variation (TTV) models are powerful tools that can encode the regional continuous structures underlying a PCT object. In a TTV model, the sparsity structures of the contrast-medium concentration (CMC) across PCT frames are assumed to be isotropic with identical and independent distribution. However, this assumption is inconsistent with practical PCT tasks wherein the sparsity has evident variations and correlations. Such modeling deviation hampers the performance of TTV-based PCT reconstructions. To address this issue, we developed a novel *c*ontrast-*m*edium *a*nisotropy-*a*ware *t*ensor *t*otal *v*ariation (CMAA-TTV) model to describe the intrinsic anisotropy sparsity of the CMC in PCT imaging tasks. Instead of directly on the difference matrices, the CMAA-TTV model characterizes sparsity on a low-rank subspace of the difference matrices which are calculated from the input data adaptively, thus naturally encoding the intrinsic variant and correlated anisotropy sparsity structures of the CMC. We further proposed a robust and efficient PCT reconstruction algorithm to improve low-dose PCT reconstruction performance using the CMAA-TTV model. Experimental studies using a digital brain perfusion phantom, patient data with low-dose simulation and clinical patient data were performed to validate the effectiveness of the presented algorithm. The results demonstrate that the CMAA-TTV algorithm can achieve noticeable improvements over state-of-the-art methods in low-dose PCT reconstruction tasks.

Keywords

Low-dose CT; image reconstruction; cerebral perfusion; tensor total variation; anisotropy sparsity

I. INTRODUCTION

CEREBRAL perfusion computed tomography (PCT) extends the role of conventional unenhanced CT and CT angiography in the evaluation of acute stroke, vasospasm, and other neurovascular disorders by providing information on capillary-level hemodynamics and the brain parenchyma [1]. PCT is critical in detecting ischemic lesions and distinguishing an infarct "core" from the hypoperfused "penumbra" [2]. However, the high level of accumulated radiation exposure from a PCT examination has been a major concern, especially when repeated scans are performed in the same patient over a long acquisition time [3]. With the ongoing introduction of full-brain PCT in many centers, the radiation exposure associated with PCT will increase even further [4]. Therefore, minimizing the radiation exposure (low radiation dose/low dose) while maintaining the quantitative accuracy of contrast-medium concentration (CMC) information in a PCT object is urgently needed in clinic [5].

There are many approaches that can reduce the radiation dose in PCT imaging, including reduction of the tube current-time product (i.e., the tube current multiplied by the exposure time per gantry rotation, mAs), reduction of the tube voltage (kVp), and increase in the intervals between PCT scans [6]. As the tube current-time product is linearly related to the radiation dose, a reduction of the tube current-time product is perhaps the simplest and most effective way to reduce radiation exposure. However, the associated PCT images are typically degraded by unavoidable noise-induced artifacts, which may hamper detection accuracy. Recent studies have shown that when using the vendor-provided filtered back-projection (FBP) or model-based image reconstruction (MBIR) methods [7], [8], a reduction of the tube current-time product to levels lower than 50 mAs substantially deteriorates the quality of perfusion information [9], [10].

One major strategy to improve the accuracy of the CMC information in low-dose PCT tasks is to estimate the high-quality hemodynamic perfusion maps from the PCT images using a stable deconvolution procedure [11], [12]. Another major strategy is to suppress the excessive noise artifacts in PCT images, for example by using image domain denoising methods and MBIR methods [13]–[18]. Image domain denoising methods mitigate noise and artifacts directly from FBP-reconstructed PCT images [13], [14]. Such postprocessing methods might suffer from diminishing clinically relevant lesions due to lack of knowledge of the data statistics, especially for ultra-low-dose cases [9]. MBIR methods model the data statistics and then optimize a prior-regularized cost function for image reconstruction by using iterative algorithms [15]–[18]. By incorporating raw data statistics into the optimization process, MBIR methods generally can achieve higher image quality compared to conventional analytical reconstruction methods [19]. Thus, MBIR reconstruction with the ability to accurately model the CMC information in a PCT object is the task in this paper.

In a PCT object, the tissue structures and lesion changes are generally regionally constant or have a low level of variation along the spatial dimension, and the variations of the blood flow signal induced by the contrast-medium concentration is generally continuous along its temporal dimension [11], [14]. Such prior structures can be readily modeled as a tensor total variation (TTV) prior [20], [21], as shown in Figs. 1(a)-(b). Multiple PCT reconstruction algorithms using such a model have been proposed, and they have shown promising performance [11], [14], [22]. In the existing TTV model, the sparsity structures of the CMC across PCT frames are formulated on the difference matrices, which are calculated along the spatial and temporal dimension (i.e., D_1, D_2, and D_3 in Fig. 1. Their definitions are introduced in detail in Sec. II). They are implicitly assumed to be isotropic with identical and independent distribution. This assumption, however, is inconsistent with practical PCT tasks. First, accounting for the tissue-heterogeneous nature of the CMC in PCT, the sparsity of the CMC in the temporal direction of the difference matrices is not identically distributed but rather exhibits evident variations, which can be clearly observed in Fig. 1(b). Second, many previous studies have confirmed that PCT frames have highly temporal correlations [17], [18], and according to the linear property of the differential operation, the sparsity of the CMC across different frames are not independent but correlated. In other words, the sparsity of the CMC across PCT frames is anisotropic with variant and correlated distribution. Such modelling deviations usually hamper the performance of TTV-based PCT reconstructions. Alleviating this problem would lead to a great improvement in PCT reconstructions.

In the past few years, considerable efforts have been invested to address the anisotropy sparsity issue in TV/TTV models. However, to the best of our knowledge, almost all of the existing methods focus on imposing some penalty weight on the TV/TTV norm to describe the different gradient magnitudes of pixel pairs. For example, Tian *et al.* [23] and Liu *et al.* [24] both proposed edge-preserving TV models that assigned a penalty weight in defining the TV term based on the negative exponential function of gradient values of adjacent pixels. Chen *et al.* [25] proposed an anisotropic TV (ATV) model by introducing a penalty weight for the TV norm based on the radial constraint strength distribution of neighboring pixels. Wang *et al.* [26] extended the ATV model by introducing an additional weight for the TV term defined as the reciprocal of the gradient magnitudes of adjacent pixels. Considering that each individual scale is sensitive to artifacts over a specific spatial range, Huang *et al.* [27] employed a reweighted TV norm at each scale space for CT reconstruction, wherein the weights were designed to be inversely proportional to the gradient magnitudes of adjacent pixels. Wu *et al.* [28] introduced the structure tensor total variation (STV) model [29] into CT reconstruction framework that defined the weighted first-order difference of a local neighborhood (called structure tensor) and imposed the nuclear norm for the structure tensor to describe the local correlation of neighborhood variations. Besides, some non-local TV/TTV models were also imposed to leverage the non-local variational information in the CT image(s). Mahmood *et al.* [30] employed a graph weight as the penalty for the TV norm, using Gaussian kernel weighting w.r.t the two patch pairs in the image. Fang *et al.* [31] proposed a non-local TTV model for the PCT deconvolution by minimizing the weighted differences between the target voxel and all voxels in a local search window where the penalty weights were defined in the same way as [30]. Although they are effective in reflecting the sparsity variations in CT image(s), these methods may be sensitive to the estimation accuracy of the penalty weight assigned to the TV term. Moreover, as they only utilize gradient information from local (or nonlocal as in [30], [31]) pixel pairs, these methods generally neglect useful global information from the difference maps, and thus cannot reflect the global sparsity correlations of the CMC across the PCT frames.

Recently, Li *et al.* [32] introduced a low-rank tensor decomposition method to describe the global correlations among PCT frames. However, the low-rank tensor decomposition model implicitly assumes that the PCT frames are free of noise for decomposition [33], which is not the case in practice. To address this problem, the authors further employed an isotropic TTV model to characterize the regional smooth structures in both the spatial and temporal domains. Although this method can address the noise problem to some extent with the TTV regularization, it may suffer from the loss of detailed CMC information due to the modeling deviation induced by the isotropic TTV. Moreover, in [32] the sinogram data were assumed to have an independent and identical Gaussian distribution, which is far from realistic in practice; as a result, the reconstructed results suffer from inhomogeneous defects, especially for ultra-low-dose cases, as demonstrated in Sec. IV. Similar to [32], Sagheer *et al.* [34] introduced a low-rank approximation method to describe the global correlations in 3D CT images by imposing the tensor nuclear norm (TNN) on similar 3D patches. Though approximation using TNN can smoothen the images, excessive and spurious noise could still remain in the resulted image [34]. To address this problem, the authors also employed the isotropic TTV model to exploits local gradient information from neighborhood pixels. As in

[32], the modeling deviation problem induced by the isotropic TTV still exists in their method. Besides, the method proposed in [34] is an image domain denoising method, which is incapable of utilizing the valuable statistics information of raw data and thus could not treat images with severe noise and artifacts.

One major goal of this research is to exploit a more advanced model to faithfully describe the intrinsic anisotropic sparsity of the CMC across PCT frames, and the other major goal is to develop an efficient algorithm for low-dose PCT reconstruction via the new model. Our contributions can be summarized as threefold:

1. We present a novel model that naturally encodes the anisotropic sparsity of the contrast-medium concentration information among the PCT frames. For ease of description, we call this model Contrast-Medium Anisotropy-Aware TTV model (CMAA-TTV). Instead of characterizing the sparsity on the difference matrices themselves as was done by the TTV model, the CMAA-TTV model formulates the sparsity on the low-rank subspace of the difference matrices, which are adaptively calculated from the input data. With the CMAA-TTV model, the sparsity correlations of the CMC are delivered by the calculated subspace bases, while the sparsity variations of the CMC are represented by their different coefficients.
2. We propose an algorithm to improve the performance of low-dose PCT reconstructions using the CMAA-TTV model. Using the alternating direction method of multipliers (ADM [35] framework, an efficient optimization method for the proposed CMAA-TTV algorithm was developed that alternates between the image update and the subspace calculation with closed-form equations.
3. We demonstrate that the proposed algorithm outperforms state-of-the-art methods in terms of noise artifact suppression and structure preservation, and that it can better represent CMC information in real clinical PCT tasks with a tube current-time product level of 20 mAs. Simulation studies demonstrate that the proposed algorithm provides more stable reconstructions at four radiation levels and yields a more accurate CMC information estimate when the tube current-time product is reduced from 50 mAs to 5 mAs, compared with other methods.

This paper is an extension of our preliminary work [36] with significant improvements: 1) we provided a more thorough analysis of the proposed model and presented the detailed algorithm for the PCT reconstruction with the model, and 2) we provided more detailed experimental results using the proposed algorithm, with extensive evaluations over both simulated data and clinical patient data.

The rest of this paper is organized as follows. In Sec. II, a brief introduction to PCT tomography modeling and the reconstruction framework is given. In Sec. III, the proposed CMAA-TTV algorithm scheme and its optimization method are presented in detail. Sec. IV evaluates the proposed method with numerical simulations and clinical patient data. Finally, the discussion and conclusion are presented in Sec. V.

II. PROBLEM FORMULATION FOR THE GENERALIZED PCT RECONSTRUCTION FRAMEWORK

A. Mathematical Notation and PCT Modeling

During acquisition, PCT is performed in cine mode a few seconds after the iodinated contrast bolus injection. The PCT object with N_t frames can be represented as a 3-order tensor $\mathscr{X} = \left\{x^t, t = 1, 2, \ldots, N_t\right\} \in \mathbb{R}^{N_h \times N_w \times N_t}$, where $x^t \in \mathbb{R}^{N_h \times N_w}$ represents the t-th 2D image frame, and N_h, N_w, and N_t denote the spatial height, width, and number of time frames respectively, as shown in Fig. 1. We denote the 2D spatial-temporal form of $\mathscr{X}$ as $\mathbf{X} = \left\{\mathbf{x}^t, t = 1, 2, \ldots, N_t\right\} \in \mathbb{R}^{(N_h N_w) \times N_t}$, where each column vector $\mathbf{x}^t \in \mathbb{R}^{(N_h N_w) \times 1}$ corresponds to the vectorized form of its corresponding image frame x^t.

For PCT modeling, we denote $\mathbf{y}^t \in \mathbb{R}^{N_d \times 1}$ as the vector of the line integral measurements that is acquired during the t-th time frame interval, and we denote $\mathbf{A}^t \in \mathbb{R}^{N_d \times (N_h N_w)}$ as the corresponding system matrix, with each element a_{ij}^t representing the contribution of voxel j to the projection ray i. Here, N_d denotes the number of measurements during a time frame interval.

Using these denotations, the PCT projection model can be defined as the following large system of linear equations

$$\mathbf{y} = \mathbf{A}\mathbf{x}, \tag{1}$$

where $\mathbf{A}$ represents the block diagonal matrix consisting of blocks $\mathbf{A}^1, \mathbf{A}^2, \ldots, \mathbf{A}^{N_t}$, and $\mathbf{y}$ and $\mathbf{x}$ represent the vertical concatenation of $\mathbf{y}^1, \mathbf{y}^2, \ldots, \mathbf{y}^{N_t}$ and $\mathbf{x}^1, \mathbf{x}^2, \ldots, \mathbf{x}^{N_t}$, respectively.

B. Statistical Reconstruction Framework for PCT

The goal of PCT image reconstruction is to estimate the desired $\mathbf{x}$ from the line integral measurements $\mathbf{y}$. Due to the presence of noise in the measurements, it is difficult to obtain a satisfactory solution by directly solving (1). Therefore, a regularization term is posed to stabilize the solution. The desired $\mathbf{x}$ can be reconstructed from the noisy measurements $\mathbf{y}$ by solving the following optimization problem:

$$\hat{\mathbf{x}} = \arg\min_{\mathbf{x}} \frac{1}{2}(\mathbf{y} - \mathbf{A}\mathbf{x})^T \mathbf{W}(\mathbf{y} - \mathbf{A}\mathbf{x}) + \beta R(\mathbf{x}), \tag{2}$$

where R(x) denotes the regularization term and the parameter β is used to control the tradeoff between the data fidelity term and the regularization term. $\mathbf{W} = diag\left\{\mathbf{W}^i\right\} \in \mathbb{R}^{(N_d N_t) \times (N_d N_t)}(i = 1, 2, \ldots, N_t)$ is the weighting matrix, where $\mathbf{W}^i \in \mathbb{R}^{N_d \times N_d}$ is a diagonal matrix with each element being the inverse variance of its corresponding measurement in $\mathbf{y}^i$, which can be determined based on our previous work [37].

A rational model with the ability to represent comprehensive prior structural knowledge of CMC in a PCT object would have great potential to boost the performance of the above reconstruction framework. This motivated us to develop a more advanced model for low-dose PCT reconstruction tasks.

III. PCT RECONSTRUCTION WITH THE PROPOSED CMAA-TTV ALGORITHM

In this section, the conventional TTV model is first reviewed in Sec. III-A. Then, the new CMAA-TTV model beyond the conventional one is described in Sec. III-B. The proposed CMAA-TTV algorithm scheme and its optimization method are introduced in Sec. III-C. The algorithm convergence behaviour and the parameter selection are described in Sec. III-D and Sec. III-E, respectively.

A. TTV Model

Let $\mathscr{D}_n(n = 1, 2, 3)$ denote the difference tensor of $\mathscr{X}$ corresponding to the spatial height, weight and temporal dimensions, respectively. As shown in Fig. 1, the three finite differential operations at voxel (h, w, t) are defined as:

$$\begin{aligned} \mathscr{D}_1(h, w, t) &= \mathscr{X}(h + 1, w, t) - \mathscr{X}(h, w, t), \\ \mathscr{D}_2(h, w, t) &= \mathscr{X}(h, w + 1, t) - \mathscr{X}(h, w, t), \\ \mathscr{D}_3(h, w, t) &= \mathscr{X}(h, w, t + 1) - \mathscr{X}(h, w, t), \end{aligned} \quad (3)$$

where $\mathscr{X}(h, w, t)$ denotes the intensity at voxel (h, w, t). Just as in Sec. II-A, we denote the 2D spatial-temporal form of $\mathscr{D}_n$ as $\mathbf{D}_n \in \mathbb{R}^{(N_h N_w) \times N_t}$. By adopting the most commonly used l_1 norm sparse measure, the TTV model for PCT can be constructed as:

$$R_{\mathrm{TTV}}(\mathbf{x}) = \sum_{n=1}^{3} \kappa_n \|\mathbf{D}_n\|_1 \quad (4)$$

where the parameters κ_n control the regularization strength for the spatial height, width and temporal dimensions, respectively.

B. CMAA-TTV Model

As the differential operations on $\mathscr{X}$ along the spatial height, width or temporal dimensions correspond to performing subtractions between rows in **x**, there exists a linear relationship between **x** and $\mathbf{D}_n$. Thus, we introduce three difference operators, Θ_n, to formulate the relationship between **x** and

$$\Theta_n \mathbf{x} = \mathbf{D}_n, n = 1, 2, 3. \quad (5)$$

This facilitates the construction of the model that is imposed on the difference matrices.

For a given PCT object **x**, we seek to model the correlated and variant sparse structures among the difference matrices, i.e., our goal is to construct a rational anisotropy sparsity measurement for $\mathbf{D}_n$. As studied in [17], [18], the intrinsic dimensionality of a PCT object is much lower than the number of acquired time frames in data acquisition (or, equivalently, there is a low-rank nature in PCT frames). Hence, according to the linear relationship between the PCT frames and the difference matrices, we can derive that $\mathbf{D}_n$ also has a low-rank property. Given this property, $\mathbf{D}_n$ can be decorrelated through the following low-rank matrix factorization form:

$$\mathbf{D}_n = \mathbf{\Omega}_n \mathbf{Z}_n^T, \tag{6}$$

where $\mathbf{\Omega}_n \in \mathbb{R}^{(N_h N_w) \times r}, \mathbf{Z}_n \in \mathbb{R}^{N_t \times r}$, and r is the rank of $\mathbf{D}_n$. Here, columns in $\mathbf{\Omega}_n$ are in fact a set of bases spanning the subspace of the data matrix $\mathbf{D}_n$, and $\mathbf{Z}_n$ contains its corresponding coefficients. We also introduce the constraints $\mathbf{Z}_n^T \mathbf{Z}_n = \mathbf{I}$ to ensure that the calculated subspace maintain compensation with the non-redundant information, where $\mathbf{I}$ is the identity matrix. With these constraints, we can rewrite (6) as follows:

$$\mathbf{\Omega}_n = \mathbf{D}_n \mathbf{Z}_n, \tag{7}$$

where $\mathbf{\Omega}_n$ can be assumed to be the linear combination of the columns of $\mathbf{D}_n$ by the coefficients in $\mathbf{Z}_n$.

Fig. 2 illustrates the basis matrix $\mathbf{\Omega}_n$ calculated from the normal-dose and the simulated low-dose PCT frames. The simulated low-dose PCT data approximately correspond to projection data acquired at 75 mAs. We can observe from Figs. 2(b) and (c) that a slight reduction of the radiation dose can seriously damage the sparsity structure of the difference images, which indicates that it is difficult to improve low-dose PCT reconstruction when using the sparsity regularization directly on the difference matrices. However, it can be observed clearly from Figs. 2(d) and (e) that the sparsity structures in $\mathbf{\Omega}_n$ are evidently less corrupted and are more stable than in the original representation $\mathbf{D}_n$. It is thus expected to be easier to recover the target PCT object x from the low-dose data via a proper regularization on $\mathbf{\Omega}_n$ than on the original $\mathbf{D}_n$ as in the TTV model.

To investigate the structural properties of $\mathbf{\Omega}_n$, we show in Fig. 3 the distribution (log scale) of absolute values in $\mathbf{\Omega}_n$. It can be seen that $\mathbf{\Omega}_n$ is sparse, with a large fraction of zero or near-zero values. Hence, we can impose $\mathbf{\Omega}_n$ to be sparse under the l_p-norm $(0 \le p < 1)$ [38]. An l_p-norm-based sparseness regularization yields a distribution with a convex shape on the logarithmic scale. From Fig. 3, we can observe that the distribution of $\mathbf{\Omega}_n$ follows this pattern. Considering that the l_p-norm problem is NP-hard [38], just similar to the general TV/TTV model, we relax the l_p-norm with the convex l_1-norm [39].

On the basis of the aforementioned analysis, the new CMAA-TTV model can be constructed with the following formulation:

$$\begin{gathered} R_{\mathrm{CMAA-TTV}}(\mathbf{x}) = \sum_{n=1}^{3} \kappa_n \|\mathbf{\Omega}_n\|_1, \\ \text{s. t.,}\ \Theta_n \mathbf{x} = \mathbf{\Omega}_n \mathbf{Z}_n^T, \mathbf{Z}_n^T \mathbf{Z}_n = \mathbf{I}, \\ \mathbf{\Omega}_n \in \mathbb{R}^{(N_h N_w) \times r}, \mathbf{Z}_n \in \mathbb{R}^{N_t \times r}. \end{gathered} \tag{8}$$

The proposed model can be easily understood from Fig. 1(c). In the CMAA-TTV model, the subspace bases $\mathbf{\Omega}_n$ and their coefficients $\mathbf{Z}_n$ are calculated from the input data adaptively.

Compared to the traditional TTV model shown in (4), the proposed model takes into account the correlation prior among the difference matrices when formulating sparsity measures. It benefits from the fact that there is a low-dimensional subspace for $\mathbf{D}_n$, which is sparse but can represent almost all information in $\mathbf{D}_n$ with a coefficient matrix $\mathbf{Z}_n$, and that the features in the subspace are more stable than those in the difference matrices themselves, especially when the PCT frames are corrupted by radiation reduction induced noise.

C. CMAA-TTV Algorithm

With the CMAA-TTV model, the cost function in (2) can be written as follows:

$$\begin{aligned} &\arg\min_{\mathbf{x}, \boldsymbol{\Omega}_n, \mathbf{Z}_n} \frac{1}{2}(\mathbf{y}-\mathbf{A}\mathbf{x})^T \mathbf{W}(\mathbf{y}-\mathbf{A}\mathbf{x}) + \beta \sum_{n=1}^{3} \kappa_n \|\boldsymbol{\Omega}_n\|_1, \\ &\text{s. t., } \boldsymbol{\Theta}_n \mathbf{x} = \boldsymbol{\Omega}_n \mathbf{Z}_n^T, \mathbf{Z}_n^T \mathbf{Z}_n = \mathbf{I}, \\ &\boldsymbol{\Omega}_n \in \mathbb{R}^{(N_h N_w) \times r}, \mathbf{Z}_n \in \mathbb{R}^{N_t \times r}, n = 1, 2, 3. \end{aligned} \tag{9}$$

In this study, we adopt the ADMM scheme [35] to solve the optimization problem in (9). In particular, the objective function in (9) can be rewritten as the following scaled augmented Lagrangian dual form:

$$\begin{aligned} \arg\min_{\mathbf{x}, \boldsymbol{\Omega}_n, \mathbf{Z}_n^T \mathbf{Z}_n = \mathbf{I}, \boldsymbol{\Gamma}_n} & \frac{1}{2}(\mathbf{y}-\mathbf{A}x)^T \mathbf{W}(\mathbf{y}-\mathbf{A}x) + \beta \sum_{n=1}^{3} \kappa_n \|\boldsymbol{\Omega}_n\|_1 \\ & + \frac{\mu}{2} \sum_{n=1}^{3} \left\|\Theta_n \mathbf{x} - \boldsymbol{\Omega}_n \mathbf{Z}_n^T + \boldsymbol{\Gamma}_n\right\|_F^2, \end{aligned} \tag{10}$$

where $\boldsymbol{\Gamma}_n$ is the Lagrangian multiplier and μ is a positive penalty scalar. (10) can be further translated into four subproblems with respect to each variable, as shown below.

1) *Subproblem for* x: Given $\{\boldsymbol{\Omega}_n, \mathbf{Z}_n, \boldsymbol{\Gamma}_n\}$, the subproblem with respect to $\mathbf{x}$ becomes

$$\begin{aligned} \mathbf{x}^{(t+1)} &= \arg\min_{\mathbf{x}} \frac{1}{2}(\mathbf{y}-\mathbf{A}\mathbf{x})^T \mathbf{W}(\mathbf{y}-\mathbf{A}\mathbf{x}) \\ &\quad + \frac{\mu}{2} \sum_{n=1}^{3} \left\|\Theta_n \mathbf{x} - \boldsymbol{\Omega}_n^{(t)} \mathbf{Z}_n^{(t)T} + \boldsymbol{\Gamma}_n^{(t)}\right\|_F^2 \\ &= \arg\min_{\mathbf{x}} \frac{1}{2}(\mathbf{y}-\mathbf{A}\mathbf{x})^T \mathbf{W}(\mathbf{y}-\mathbf{A}\mathbf{x}) + R_1(\mathbf{x}) \end{aligned} \tag{11}$$

where $R_1(\mathbf{x})$ represents the second term of the above equation.

The large scale of the system matrix $\mathbf{A}$ makes it impractical to directly solve the problem (11). In this study, we employ the recently developed relaxed linearized augmented Lagrangian method with ordered-subsets acceleration (OS-LALM) [41] to solve such a problem given its advantage of fast convergence, as shown in Algorithm 1. For the proposed CMAA-TTV regularization model, the relaxed OS-LALM is well suited because that the diagonal majorizing matrix of the Hessian of $R_1(\mathbf{x})$ is a constant term that can be cheaply precomputed before the iteration. Specifically, the gradient of $R_1(\mathbf{x})$ in (11) is

$$\nabla R_1(\mathbf{x}) = \mu \sum_{n=1}^{3} \Theta_n^*\left(\Theta_n\mathbf{x} - \boldsymbol{\Omega}_n^{(t)}\mathbf{Z}_n^{(t)T} + \boldsymbol{\Gamma}_n^{(t)}\right), \tag{12}$$

where Θ_n^* is the adjoint operator of Θ_n (mathematically, $\Theta_n^*\mathbf{x}$ corresponds to the 2D spatial-temporal form of $\mathcal{D}_n^*$, where $\mathcal{D}_n^* = -\mathcal{D}_n$). $\boldsymbol{\Psi}_R$ is a diagonal majorizing matrix of the Hessian of R_1(x), specifically:

$$\boldsymbol{\Psi}_R \triangleq \mu \sum_{n=1}^{3} diag\left\{\left|\Theta_n^*\right|\left|\Theta_n\right|\mathbf{1}\right\} \geq \mu \sum_{n=1}^{3} \Theta_n^*\Theta_n = \nabla^2 R_1(\mathbf{x}) \tag{13}$$

where $|\cdot|$ is the elementwise absolute operation. For the case of the 1-order difference operation in this study, each row in Θ_n or Θ_n^* constrains two nonzero items (i.e., 1 and −1). Thus, we can easily obtain $\left|\Theta_n^*\right|\left|\Theta_n\right|\mathbf{1} = 4 \cdot \mathbf{1}$. As a result, $\boldsymbol{\Psi}_R \triangleq \mu\sum_{n=1}^{3} diag\left\{\left|\Theta_n^*\right|\left|\Theta_n\right|\mathbf{1}\right\} = 12\mu\mathbf{I}$ is a constant term. In Algorithm 1, the matrix $\boldsymbol{\Psi}_{\mathrm{A}}$ is a diagonal majorizing matrix of $\mathbf{A}^T\mathbf{WA}$. As in [41], we use

$$\boldsymbol{\Psi}_{\mathrm{A}} \triangleq diag\left\{\mathbf{A}^T\mathbf{WA1}\right\} \tag{14}$$

where $\mathbf{1}$ is an all-ones vector with proper dimensionality. The definitions of the other symbols in Algorithm 1 are the same as those used in [41]: K is the iteration number; M is the ordered subset number; $\alpha \in [1, 2)$ is the relaxation parameter; $\mathbf{A}_m$, $\mathbf{W}_m$, and $\mathbf{y}_m$ are the subvectors corresponding to the m-th subset of $\mathbf{A}$, $\mathbf{W}$, and $\mathbf{y}$, respectively; and the parameter ρ decreases gradually with the iteration:

$$\rho_t(\alpha) = \pi/\alpha(t+1)\sqrt{1-(\pi/2\alpha(t+1))^2}, t \geq 1. \tag{15}$$

2) *Subproblem for* $\boldsymbol{\Omega}_n$: Given $\{\mathbf{x}, \mathbf{Z}_n, \boldsymbol{\Gamma}_n\}$, the subproblem with respect to $\boldsymbol{\Omega}_n$ becomes

$$\begin{aligned}\boldsymbol{\Omega}_n^{(t+1)} = {} & \underset{\boldsymbol{\Omega}_n}{\operatorname{argmin}} \beta\kappa_n\left\|\boldsymbol{\Omega}_n\right\|_1 \\ & + \frac{\mu}{2}\left\|\Theta_n\mathbf{x}^{(t+1)} - \boldsymbol{\Omega}_n\mathbf{Z}_n^{(t)T} + \boldsymbol{\Gamma}_n^{(t)}\right\|_F^2 .\end{aligned} \tag{16}$$

On the basis of the orthogonal property of $\mathbf{Z}n$, (16) can be transformed as

$$\begin{aligned}\boldsymbol{\Omega}_n^{(t+1)} = {} & \underset{\boldsymbol{\Omega}_n}{\operatorname{argmin}} \beta\kappa_n\left\|\boldsymbol{\Omega}_n\right\|_1 \\ & + \frac{\mu}{2}\left\|\boldsymbol{\Omega}_n - \left(\Theta_n\mathbf{x}^{(t+1)} + \boldsymbol{\Gamma}_n^{(t)}\right)\mathbf{Z}_n^{(t)}\right\|_F^2 .\end{aligned} \tag{17}$$

This problem can be cheaply solved by the soft thresholding

Algorithm 1

CMAA-TTV

```
Input: $\mathbf{y}, \mathbf{W}, \mathbf{A}, \mathbf{x}^{(0)} = \mathrm{FBP}(\mathbf{y}), \boldsymbol{\Omega}_n = \mathbf{0}, \mathbf{Z}_n = \mathbf{0}, \boldsymbol{\Gamma}_n = \mathbf{0}, r, \tau_n\left(\overset{\Delta}{=} \beta\kappa_n\right), \mu, \alpha = 1.999, M = 12.$
Output: the reconstructed PCT image $\mathbf{x}$.
for $t = 0$ to $T - 1$ do
    Update $\mathbf{x}$ by the relaxed OS-LALM:
        initialization
        $\rho = 1, \tilde{\mathbf{x}}^{(0)} = \mathbf{x}^{(t)}, \mathbf{g}^{(0)} = \zeta^{(0)} = M\mathbf{A}_m^T\mathbf{W}_m\left(\mathbf{A}_m\mathbf{x}^{(0)} - \mathbf{y}_m\right), \mathbf{h}^{(0)} = \boldsymbol{\Psi}_\mathrm{A}^{(0)}\mathbf{x}^{(0)} - \zeta^{(0)}.$
        for $k = 0$ to $K - 1$ do
            for $m = 0$ to $M - 1$ do
                $r = kM + m,$
                $\mathbf{s}^{(r+1)} = \rho\left(\boldsymbol{\Psi}_\mathrm{A}\tilde{\mathbf{x}}^{(r)} - \mathbf{h}^{(r)}\right) + (1 - \rho)\mathbf{g}^{(r)},$
                $\tilde{\mathbf{x}}^{(r+1)} = \left[\tilde{\mathbf{x}}^{(r)} - (\rho\boldsymbol{\Psi}_\mathrm{A} + \boldsymbol{\Psi}_R)^{-1}\left(\mathbf{s}^{(r+1)} + \nabla R_1\left(x^{(r)}\right)\right)\right]_+,$
                $\zeta^{(r+1)} = M\mathbf{A}_m^T\mathbf{W}_m\left(\mathbf{A}_m\tilde{\mathbf{x}}^{(r+1)} - \mathbf{y}_m\right),$
                $\mathbf{g}^{(r+1)} = \frac{\rho}{\rho + 1}\left(\alpha\zeta^{(r+1)} + (1 - \alpha)\mathbf{g}^{(r)}\right) + \frac{1}{\rho + 1}\mathbf{g}^{(r)},$
                $\mathbf{h}^{(r+1)} = \alpha\left(\boldsymbol{\Psi}_\mathrm{A}\tilde{\mathbf{x}}^{(r+1)} - \zeta^{(r+1)}\right) + (1 - \alpha)\mathbf{h}^{(r)},$
                decrease $\rho$ using (15).
            end for
        end for
        $\mathbf{x}^{(t+1)} = \tilde{\mathbf{x}}^{(KM)}.$
    Update $\boldsymbol{\Omega}_n$ by (18).
    Update $\mathbf{Z}_n$ by (21).
    Update $\boldsymbol{\Gamma}_n$ by (22).
end for
```

method [35]:

$$\boldsymbol{\Omega}_n^{(t+1)} = S_{\beta\kappa_n/\mu}\left(\left(\Theta_n\mathbf{x}^{(t+1)} + \boldsymbol{\Gamma}_n^{(t)}\right)\mathbf{Z}_n^{(t)}\right) \tag{18}$$

where

$$S_\Delta(a) = \begin{cases} a - \Delta, & if\ a > \Delta, \\ a + \Delta, & if\ a < -\Delta, \\ 0, & otherwise. \end{cases} \tag{19}$$

3) *Subproblem for $\mathbf{Z}_n$*: Given $\{\mathbf{x}, \boldsymbol{\Omega}_n, \boldsymbol{\Gamma}_n\}$, the subproblem with respect to $\mathbf{Z}_n$ becomes

$$\mathbf{Z}_n^{(t+1)} = \underset{\mathbf{Z}_n^T\mathbf{Z}_n = \mathbf{I}}{\arg\min} \frac{\mu}{2}\left\|\Theta_n\mathbf{x}^{(t+1)} - \mathbf{\Omega}_n^{(t+1)}\mathbf{Z}_n^T + \mathbf{\Gamma}_n^{(t)}\right\|_F^2. \tag{20}$$

The closed-form solution of (20) can be obtained by the following formula:

$$\mathbf{Z}_n^{(t+1)} = \mathbf{B}_n\mathbf{C}_n^T, \tag{21}$$

where $\left(\Theta_n\mathbf{x}^{(t+1)} + \mathbf{\Gamma}_n^{(t)}\right)^T\mathbf{\Omega}_n^{(t+1)} = \mathbf{B}_n\mathbf{\Sigma}_n\mathbf{C}_n^T$ is the SVD decomposition of $\left(\Theta_n\mathbf{x}^{(t+1)} + \mathbf{\Gamma}_n^{(t)}\right)^T\mathbf{\Omega}_n^{(t+1)}$. The proof is presented in APPENDIX A.

4) ***Subproblem for*** **Γ*n*:** Under the ADMM framework, the Lagrangian multipliers can be updated as follows:

$$\mathbf{\Gamma}_n^{(t+1)} = \mathbf{\Gamma}_n^{(t)} + \left(\Theta_n\mathbf{x}^{(t+1)} - \mathbf{\Omega}_n^{(t+1)}\mathbf{Z}_n^{(t+1)T}\right). \tag{22}$$

The overall flowchart for the proposed CMAA-TTV algorithm is presented in Algorithm 1. The algorithm alternates between estimating the subspace bases $\mathbf{\Omega}n$ and their coefficients $\mathbf{Z}n$, and using these estimations to obtain an improved PCT object $\mathbf{x}$ (that also complies with the original measurements $\mathbf{y}$).

D. Algorithm Convergence Behaviour

The algorithm stops after a maximum number of iterations is reached. Otherwise, the algorithm terminates when the following criteria are satisfied: if $\|\mathbf{x}^{(t+1)} - \mathbf{x}^{(t)}\|_F / \|\mathbf{x}^{(t)}\|_F \le \epsilon$, and $\left\|\Theta_n\mathbf{x}^{(t+1)} - \mathbf{\Omega}_n^{(t+1)}\mathbf{Z}_n^{(t+1)T}\right\|_F \le \epsilon$ hold, the corresponding optimization ends. Here, ϵ is a prefixed threshold and was set as 10^{-3} in our experiments. We empirically find that the combination of the two stop strategies can consistently lead to satisfactory results. Whether the iterates in the CMAA-TTV algorithm converge to the critical points remains to be investigated further. Although theoretical convergence is not guaranteed, the decreasing tendency of the objective value at a global scale in iteration could be observed in all our experiments. For example, we conducted multiple repetitions of the digital brain perfusion phantom as described in Sec. IV-A to empirically validate the convergence behaviour of the proposed CMAA-TTV algorithm. In specific, the noisy projection data of this phantom were generated 200 times using the technique described in Sec. IV-A with $I_0 = 5 \times 10^3$ and $\sigma_e^2 = 16$, then the data were reconstructed using the proposed algorithm, and the mean values of the root mean square error (RMSE) were calculated. Besides, we also generated and reconstructed the phantom data using the same way as above with the incident flux gradually reduced down from 5×10^3 to 1×10^3 to further explore the performance limit of the proposed algorithm (σ_e^2 was fixed at 16). The results were depicted by the curve in Fig. 4. It can be observed that *1)* All the RMSE curves are monotonically decreasing for the five dosage levels. Even though the incident flux is down to 1×10^3, such monotonous descent tendency still holds. *2)* For all dose levels, approximately 40 iterations can produce relatively stable solution without the noticeable performance improvement after further iterations. *3)*

When the incident flux was reduced from 5 × 10^3 to 2 × 10 ^{3}, the final resulted RMSE increased by less than 1.3. But when the incident flux was reduced down to 1 × 10^3, the final resulted RMSE dramatically increased to as high as 6.14. This demonstrates that the proposed algorithm could work well for the data with the incident flux level above 2 × 10^3, while would degrade noticeable for the data with the incident flux level below 2 × 10^3.

E. Parameter Selection

The parameters in the proposed CMAA-TTV algorithm include the regularization coefficients $\tau_n\left(\overset{\Delta}{=}\beta\kappa_n\right)$, the penalty scalar μ, and the rank r.

The parameters $\boldsymbol{\tau}_n$ control the trade-off between the data fidelity term and the CMAA-TTV regularization term. Large values of $\boldsymbol{\tau}_n$ would achieve very low sparsities of the low-rank subspace and reduce the noise but potentially oversmooth the images and obscure fine structures. In this study, the values of $\boldsymbol{\tau}_n$ were set as $\tau_1 = \tau_2 = 0.9\tau_3 = C\sqrt{N_hN_w}$, where C needs to be tuned depending on the empirical data. In implementation, the C value in the digital brain perfusion phantom experiments was set as 2500, and that in both the simulated and real patient data experiments was set as 30000. μ is a Lagrangian penalty parameter introduced by the ADMM algorithm which also should be tuned to achieve satisfactory performance.

The rank r corresponds to the dimensionality of the calculated low-rank subspace for the difference matrix $\mathbf{D}_n$. A proper rank is essential for the proposed algorithm to function well. To investigate the influence of the rank on the algorithm, we illustrate in Fig. 5 the RMSE and the structural similarity index (SSIM) [42] values of the PCT images reconstructed by the proposed CMAA-TTV algorithm for the digital brain perfusion phantom with different rank versus different simulated radiation levels when fixing other parameters. For all dose levels, the quantitative results followed similar trends with respect to the varying rank parameters. The quantitative accuracies of the reconstructed images degrade obviously when the rank is less than 8. We think the reason is that the calculated subspace with such small dimensionality would lose significant information contained in the original data space. The algorithm performs well when the rank ranges from 8 to15. When using a rank within the range of 8 to 15, the SSIM and RMSE vary by less than 0.001 and 0.026. When the rank increases from 15, the gradual decline of the algorithm performance could be observed. We think this is because that although the calculated subspace with a large dimensionality could represent more information contained in the original data space, it would contain more undesired information and the features in such subspace thus would be more susceptible to the artifacts noise.

IV. EXPERIMENTAL RESULTS

In this section, we evaluated the proposed CMAA-TTV algorithm by using one digital brain perfusion phantom, 22 low-dose simulation datasets and data from seven patients who underwent low-dose PCT. For comparison, the performance of analytical reconstruction with the FBP algorithm, and the recently developed state-of-the-art MBIR algorithms, including TTV [11] and LRTD-STTV [32], were also evaluated. The performance of other MBIR algorithms, such as tensor-based dictionary learning (TDL) regularization [43], low-rank and total variation (LRTV) regularization [14], total variation with feature refinement (TV-FR) regularization [44], and normal-dose scan-induced structure tensor total variation (ndiSTV) regularization [45] are inferior to LRTD-STTV as demonstrated in [32] and thus omitted here. We also compared the performance of the proposed algorithm with the DP-ResNet algorithm [46], a state-of-the-art deep learning algorithm which is a progressive 3D residual convolution network whose structure contains sinogram domain network, filtered back projection and image domain network. We trained the network with normal-dose patient data and simulated low-dose patient data pairs using the mini-batch version of Adam [47]. Since the digital brain phantom does not contain the skull and the voxel values of this digital phantom fall far different numeric range from the actual voxel values of the clinical CT images, we only evaluted the DP-ResNet algorithm with the simulated low-dose patient data and the real low-dose patient data as described in Sec. IV-B and Sec. IV-C. Detailed parameters used for the TTV, LRTD-STTV and DP-ResNet algorithms could be found in the supplemental material. The proposed CMAA-TTV algorithm will be available at https://github.com/Frank-ZhangYK/CMAA-TTV.

A. Digital Brain Perfusion Phantom Study

1) Data Acquisition: A digital brain perfusion phantom consisting of user-defined regions of penumbra and stroke core [15] was used as a numerical reference, as shown in Fig. 6(a). The phantom contains 40 temporal frames of size 256 × 256. In all simulations, a fan-beam CT geometry was used with imaging parameters that were the same as those of the GE CT scanner, i.e., 984 fan-beam projections for a 360° rotation, 888 bins for each projection view, detector cell spacing of 1.0239 mm, distance of 949.075 mm from the X-ray source to the detector arrays, and distance of 541 mm from the X-ray source to the center of rotation. To simulate the noisy measurements, we added noise to the noise-free measurements by using the simulation method described in Ref. [37]:

$$I_N \sim \text{ Poisson } \{I_0 \exp(-[\mathbf{Ax}]_i)\} + \text{Gaussian}\left\{0, \sigma_e^2\right\}, \tag{23}$$

where σ_e^2 denotes the electronic background noise variance and is set to 16, and I_0 denotes the incident flux and is deliberately selected to be 5×10^4, 2×10^4, 1×10^4 and 5×10^3 for approximately four matching tube current-time products levels, which correspond to 50, 20, 10 and 5 mAs, respectively. The detailed description about the low-dose simulation method is presented in the supplementary materials.

2) Visual Evaluation: Fig. 6(b) shows the reconstructed results of one representative PCT frame (#17) of the digital phantom versus the radiation level. Severe noise and artifact are evident in the FBP reconstructions, and they increase substantially as the radiation level is reduced. At 50 mAs, all of the MBIR algorithms can suppress the noise and preserve the fine structures effectively. However, as the radiation level was further reduced, especially in ultra-low-dose scenarios (with a tube current-time product below 20 mAs), the TTV and LRTD-STTV algorithms tend to blur some meaningful structures around both the penumbra and stroke core regions. By formulating a more insightful sparsity structure of the CMC, the proposed algorithm provides more stable performance at various dose levels; moreover, it provides much better reconstruction results in terms of both noise artifact suppression and fine structure preservation, as shown in Fig. 6(b), especially for the ROIs of both the penumbra and the stroke core (as shown in Fig. 6(c)).

3) Quantitative Evaluation: The performance of the proposed algorithm was quantitatively evaluated in terms of the RMSE and the SSIM measurements of a region containing both the penumbra and stroke core (ROI I, as marked by the red dotted rectangle in Fig. 6(a)). The corresponding results are shown in Fig. 7. The CMAA-TTV exhibited the best quantitative results, with the lowest RMSE and the highest SSIM. For all algorithms, the RMSE rises and the SSIM drops as the radiation level decreases, but this effect was less pronounced in the CMAA-TTV results (RMSE of 0.45, 0.73, 1.12, 1.66 and SSIM of 0.9982, 0.9959, 0.9927, and 0.9869 at 50, 20, 10 and 5 mAs, respectively).

4) Hemodynamic Parameter Map Evaluation: In PCT, the hemodynamic parametric maps have the ability to exhibit perfusion deficits in a smaller brain territory. The commonly used hemodynamic parametric maps include the cerebral blood flow (CBF), cerebral blood volume (CBV), and mean transit time (MTT). In this study, we estimated the maps from the reconstructed PCT images using the bSVD deconvolution algorithm [48]. The perfusion maps obtained with the tube current-time product of 5 mAs are shown in Fig. 8 (the perfusion maps obtained at 50, 20, and 10 mAs are shown in the supplementary materials). The quantitative accuracy of the maps was measured by the RMSE and the SSIM metric,, as shown in Table I.

At every dose level, all of the MBIR algorithms provided more accurate estimates of the CMC information than the FBP algorithm. From 50 mAs to 20 mAs, the TTV, LRTD-STTV and CMAA-TTV algorithms all performed well in estimating the maps. However, when the tube current-time product was reduced below 20 mAs, the CMAA-TTV algorithm estimated the maps with higher accuracy than the other algorithms.

5) Time Density Curve (TDC) Measures: The TDC describes the progression of local CMC over time, which is a crucial quantitative measurement for accurate perfusion therapy. Fig. 9 shows the averaged TDCs in two representative ROIs (the penumbra ROI indicated by the small green box, and the stroke core ROI indicated by the small yellow box, as shown in Fig. 6(a)) from reference images and low-dose PCT images reconstructed using different algorithms at 5 mAs (the TDCs at 20 mAs and 10 mAs are shown in the supplementary materials). The reconstruction obtained with the proposed CMAAReference TTV algorithm matches the ground truth for both selected ROIs much better than other methods, especially in ultra-lowdose scenarios (10 mAs and 5 mAs). The results indicate that the proposed algorithm performs better in preserving perfusion information for both the penumbra and the stroke core.

B. Clinical Patient Data with Low-dose Simulation

1) Data Acquisition: In this study, twenty-two patients with brain deficits were recruited under informed consents after approval from the institutional clinical trials review board. The patients were first injected with a 50 mL bolus of nonionic iodinated contrast via a power injector at a rate of 5 mL/s. Then, normal-dose PCT images consisting of 30 volumetric scans were acquired 5 seconds after injection, using a Siemens multi-slice CT scanner at an X-ray tube voltage of 80 kVp and a tube current-time product of 200 mAs. Other parameters of the scanning protocol for each volumetric scan were as follows: slice thickness of 8 mm, 1 s per rotation, helical pitch of 1, and frame size of 512 × 512 mm. To reduce the radiation dose, instead of scanning the patients twice, we simulated the low-dose PCT data from the FBP reconstructed PCT images. The simulation technique is similar to that described in section IV-A. I_0 and σ_e^2 were selected to be 1×10^4 and 25 respectively.

For the DP-ResNet algorithm, cross-validation was utilized in the testing phase for fairness. While testing on 3D PCT frames from each patient, the 3D PCT frames from other 21 patients were involved in the training phase. The original DP-ResNet was applied on the 3D volume scans (in practice on the decomposed 3D rectangular patches with size $h_p \times w_p \times d_p$ for memory saving, where h_p, w_p, d_p are the height, width and slice depth of the data). Because the proposed CMAA-TTV model is applied on the 3D PCT objects, for a fair comparison we modified the DP-ResNet by feeding the 3D PCT objects (in practice the decomposed 3D PCT patches) into the network during the training. With such modification, the DP-ResNet can also exploit the correlated information across temporal frames.

2) Visual Evaluation: Fig. 10 illustrates the reconstructed results obtained by different algorithms for one representative PCT frame (frame 12) from a patient (referred to as patient #S1). The reconstructed results for another frame (frame 8) from the same patient are shown in the supplementary materials. The reconstructed results from another patient (referred to as patient #S2) are also shown in the supplementary materials. All of the algorithms were able to suppress the noise artifacts effectively. However, the deviation of the model from the empirical CMC data caused both the TTV and the LRTD-STTV algorithms to blur some meaningful structures. Moreover, the LRTD-STTV algorithm tended to generate results with obviously inhomogeneous effects. We think that this may be due to deviations between the model and the sinogram data: the model assumes that the sinogram data have an independent and identical Gaussian distribution, rather than a non-stationary Gaussian distribution as we used in (2). The DP-ResNet algorithm can remove the noise and artifacts, but it tends to generate results with blurred CMC structures. We think that this may be due to the following two reasons: *1)* Although the DP-ResNet contains both the sinogram domain network and the image domain network which can improve the complete imaging pipeline from low-dose projection into CT images, the two sub-networks are in fact separated by the FBP operation and are thus completely independent. Such hybrid domain network is generally empirical with no rigorous mathematical derivation, which might limit its performance. *2)* Although the DP-ResNet can learn the correlated information across temporal frames by the 3D convolution, its leaning ability would be restricted by the limited receptive field along the temporal dimensionality. As a result, the DP-ResNet would be hard to exploit global correlations among PCT frames, and thus is deficient to represent the global anisotropic correlated structures of the CMC. The proposed CMAA-TTV performs much better in terms of both noise artifact suppression and preservation of fine structures compared with other methods, and it produces a visual effect that is similar to the normal-dose reference, especially for the ROI of the suspected ischemic lesion (as marked by the arrows in Fig. 10).

3) Hemodynamic Parameter Map Evaluation:

The hemodynamic parametric maps from the normal-dose and low-dose PCT images reconstructed by different algorithms were estimated. To save space, we show only the CBF maps for patient #S1 in Fig. 11 and show the CBF, CBV and MTT maps for patients #S1 and #S2 in the supplementary materials. The quantitative accuracy of the maps are measured by the RMSE and the SSIM metrics. In specific, we calculated the RMSE and SSIM of the maps from each patient, and then calculated the mean value and the SDs of the SSIM values of all the patients. The average RMSE and SSIM accuracies (mean±SDs) of the perfusion maps are listed in Table I. All of the algorithms provided more quantitative accurate estimates of the CMC information than the FBP algorithm. In particular, the CMAA-TTV method estimated the CMC information with significantly higher accuracy than other algorithms.

4) TDC Measures:

Fig. 12 shows the averaged TDCs in two representative ROIs (the ROI with relatively low levels of CMC that is indicated by the small green box, and the ROI with relatively high levels of CMC that is indicated by the small yellow box, as shown in Fig. 10) from the reference and low-dose PCT frames of patient #S1, as reconstructed using different algorithms. The reconstruction obtained with the proposed CMAA-TTV algorithm matches the ground truth for both selected ROIs much better than other methods. The results indicate that the proposed algorithm performs better in preserving perfusion information for regions with both low and high contrast-medium concentrations.

C. Clinical Data Study

1) Data Acquisition:

Seven patients with brain deficits were recruited after obtaining informed consent and approval from the institutional clinical trials review board. A 45 mL bolus of nonionic iodinated contrast was administered via a power injector at a rate of 4 mL/s. Twenty-seven low-dose PCT volumetric scans were acquired 5 seconds after injection using a CT scanner at an X-ray tube voltage of 80 kVp and a tube current-time product of 20 mAs. Other parameters of the scanning protocol for each volumetric scan were as follows: slice thickness of 5 mm, 0.4 s per rotation, and frame size of 512×512 mm. FBP reconstruction with a commercial kernel “Std” was used as a vendor-based reconstruction result for comparison.

For these clinical low-dose patient data, we also reconstructed the PCT images using the DP-ResNet algorithm which was trained using paired training data (as described in section IV-B) which were simulated at dose level of 20 mAs, and compared the performance of DP-ResNet with the proposed CMAA-TTV.

2) Visual Evaluation:

Fig. 13 shows the reconstructed results obtained with different methods for one representative frame (frame 15) from a patient (referred to as patient #C1). The reconstructed results for another representative frame (frame 20) from the same patient are shown in the supplementary materials. The reconstructed results from another patient (referred to as patient #C2) are shown in the supplementary materials. When using real clinical data, the proposed CMAA-TTV algorithm performs much better than the TTV, LRTD-STTV and DP-ResNet algorithms with respect to both noise artifact suppression and structural preservation.

3) Evaluation by Radiologists: The hemodynamic parametric maps from the reconstructed PCT images of the 7 patients were estimated. Due to space constraints, we show the CBF maps for patient #C1 in Fig. 14 (the CBF, CBV and MTT maps for patients #C1 to #C2 are shown in the supplementary materials). Again, all of the MBIR algorithms provided more accurate map estimates than the FBP algorithm.

Furthermore, we reconstructed three randomly selected slices from each patient's volumetric scans using the different reconstruction methods (i.e., we had three PCT objects for each patient), and calculated their CBF, CBV and MTT maps. Then three experienced radiologists were employed to evaluate these perfusion maps. In specific, the CBF, CBV and MTT maps from the same PCT object were first stored as a map group. Then all the map groups were scored independently by the three radiologists based on their overall impression of the three maps, in terms of noise artifact reduction, structural preservation and estimation of the ischemic lesion. For a fair comparison, we mixed all of the map groups and displayed them on the screen randomly for each radiologist, and they were scored one by one. The scores ranged from 0 (worst) to 5 (best). The resulting scores (mean±SDs) are reported in Table II. The proposed CMAA-TTV algorithm has significant advantages over other methods in terms of subjective assessment scores. In conclusion, the proposed algorithm can achieve better results than other state-of-the-art methods for the reconstruction of real clinical low-dose PCT data.

V. Discussion and Conclusion

Rather than being independent and identical distributed, the intrinsic sparsity structures of the CMC across all PCT frames are variant and correlated. To characterize such anisotropic sparsity configurations, a novel contrast-medium anisotropy-aware TTV (CMAA-TTV) model was developed in this study. In the CMAA-TTV model, we took advantage of the low-rank nature of the difference maps to establish the sparsity correlation among PCT frames, and we imposed the sparsity measure on a low-rank subspace, which were obtained by the linear combination of the original gradient vectors along PCT frames with a coefficient matrix. This new measure rationally characterizes the correlations and variations among the sparsity structures of the CMC. Specifically, the CMC sparsity correlations across the PCT frames can be formulated as the calculated low-rank subspace bases, and the coefficients represent the CMC sparsity variations. The additional advantage of structural stability of the subspace makes the sparsity measures less susceptible to noise induced by radiation reduction.

We also proposed a novel algorithm based on the CMAA-TTV model, which we named CMAA-TTV, to improve the performance of low-dose PCT reconstructions. In the proposed CMAA-TTV algorithm, an alternating minimization method is developed to solve the joint optimization problem. The algorithm alternates between the image update step and the subspace calculation step. We have implemented the proposed algorithm using MATLAB on a Linux OS with a PC workstation configured with an Intel CPU (8 cores, 3.4 GHz) and 64G of RAM. Without using any parallel technique, the algorithm took approximately 280 seconds to process real clinical perfusion data with a size of $512 \times 512 \times 27$ at each iteration step. As a comparison, the TTV algorithm [22] took approximately 260 seconds for one iteration for the same PCT object, while the LRTD-STTV algorithm [32] took approximately 1100 seconds. As an iterative reconstruction method, the proposed CMAA-TTV algorithm took more time than the deep learning based algorithm. In the future, GPU-assisted implementation will be developed, and is expected to dramatically accelerate the implementation of the algorithm for possible clinical use.

Both numerical simulations and clinical patient data were used to evaluate the proposed algorithm. The results indicate that the proposed algorithm led to noticeable improvements over state-of-the-art algorithms in terms of noise artifact suppression, structure preservation and representation of CMC information. Simulation studies also demonstrate that even when the tube current-time product level was reduced to ultra-low-dose level (such as the incident flux was reduced to lower than 1×10^4), the CMAA-TTV algorithm still yielded quite accurate estimations of CMC information.

It is worth noting that the number of time points (i.e., frame numbers in a PCT object) can affect the performance of the proposed algorithm. In clinical PCT exams, the number of frames is usually greater than 15 (with temporal sampling intervals of 0.5 to 3 seconds over the whole scan durations to capture the complete venous first pass [50], [51]), and the proposed algorithm works well in such cases. However, as the intervals between scans continue to increase, the performance of the CMAA-TTV algorithm gradually declines. One possible reason is that as the sampling intervals increase, the correlation between PCT frames becomes weaker and the structure differences between adjacent frames become greater. Thus, the low-rank property of PCT frames is no longer satisfied. As a result, the proposed algorithm may be invalid if it still imposes sparsity regularization on the basis matrix derived from the low-rank factorization of the difference maps of PCT frames.

In this study, the CMAA-TTV model is developed for the 3D PCT object which represents the perfusion information in a particular slice location. With proper tensor unfolding operation, the presented CMAA-TTV model can also be imposed on a 4D PCT object to characterize the overall perfusion information in all slice locations. Further performance improvements with such 4D model could be expected. However, a major concern of the 4D model is the high computational load compared with the 3D model. How to reduce the computational complexity of the 4D model is an important issue and is worthy of being investigated further.

The proposed CMAA-TTV model and CMAA-TTV algorithm can be used in other medical imaging tasks such as dynamic myocardial perfusion CT imaging [52], spectral CT imaging [53], dynamic positron emission tomography (PET) imaging [54], and dynamic magnetic resonance (MR) imaging [55]. This will be another research focus in our future work.

Supplementary Material

Refer to Web version on PubMed Central for supplementary material.

Acknowledgments

This work was supported in part by the National Natural Science Foundation of China under Grants 61871383 and U1708261, in part by the China Postdoctoral Science Foundation under Grant 2020M672710, and in part by the NIH/NCI grant #CA206171.

APPENDIX A: Proof of the Updating Formula for Zn in Eq. (21)

Proof:

On the basis of the orthogonal property of $\mathbf{Z}_n$ and the property of the Frobenius norm, Eq. (20) can be transformed as

$$\mathbf{Z}_n^{(t+1)} = \underset{\mathbf{Z}_n^T\mathbf{Z}_n = \mathbf{I}}{\arg\min} \left\langle \left(\Theta_n \mathbf{x}^{(t+1)} + \mathbf{\Gamma}_n^{(t)}\right)^T \mathbf{\Omega}_n^{(t+1)}, \mathbf{Z}_n \right\rangle, \quad \text{(a1)}$$

where $\langle \cdot, \cdot \rangle$ is the inner product. The closed-form solution of Eq. (a1) can be obtained by the following theorem [33]:

Theorem 1.

$\forall \mathbf{Q} \in \mathbf{R}^{m \times n}$, *the following problem:*

$$\min_{\mathbf{Z}^T\mathbf{Z} = \mathbf{I}} \langle \mathbf{Q}, \mathbf{Z} \rangle \quad \text{(a2)}$$

has the closed-form solution $\widehat{\mathbf{Z}} = \mathbf{B}\mathbf{C}^T$, *where* $\mathbf{Q} = \mathbf{B}\mathbf{\Sigma}\mathbf{C}^T$ *is the SVD decomposition of* $\mathbf{Q}$.

Therefore, we can update $\mathbf{Z}n$ by the following formula:

$$\mathbf{Z}_n^{(t+1)} = \mathbf{B}_n\mathbf{C}_n^T, \quad \text{(21)}$$

where $\left(\Theta_n \mathbf{x}^{(t+1)} + \mathbf{\Gamma}_n^{(t)}\right)^T \mathbf{\Omega}_n^{(t+1)} = \mathbf{B}_n\mathbf{\Sigma}_n\mathbf{C}_n^T$ is the SVD decomposition of $\left(\Theta_n \mathbf{x}^{(t+1)} + \mathbf{\Gamma}_n^{(t)}\right)^T \mathbf{\Omega}_n^{(t+1)}$. ■

References

[1]. Shetty SK and Lev MH, "CT perfusion in acute stroke," Neuroimag. Clin. N. Am, vol. 2005, no. 15, pp. 481–501, 2005.

[2]. Konstas AA, Goldmakher GV, Lee TY, and Lev MH, "Theoretic basis and technical implementations of CT perfusion in acute ischemic stroke, part I: Theoretic basis," Am. J. Neuroradiol, vol. 30, no. 5, pp. 885–892, 2009. [PubMed: 19299489]

[3]. Wintermark M and Lev MH, "FDA investigates the safety of brain perfusion CT," AJNR Am. J. Neuroradiol, vol. 31, no. 1, pp. 2–3, 2010. [PubMed: 19892810]

[4]. Manniesing R, Oei MTH, Ginneken BV, and Prokop M, "Quantitative dose dependency analysis of whole-brain CT perfusion imaging," Radiology, vol. 278, no. 1, pp. 190–197, 2016. [PubMed: 26114226]

[5]. Pearce MS, Salotti JA, Little MP, McHugh K, Lee C, Kim KP, Howe NL, Ronckers CM, Rajaraman P, Craft SAW, Parker L, and González AB, "Radiation exposure from CT scans in

childhood and subsequent risk of leukaemia and brain tumours: a retrospective cohort study," Lancet, vol. 380, no. 9840, pp. 499–505, 2012. [PubMed: 22681860]

[6]. Othman AE, Afat S, Brockmann MA, Nikoubashman O, Brockmann C, Nikolaou K, and Wiesmann M, "Radiation dose reduction in perfusion CT imaging of the brain: A review of the literature," J. Neuroradiology, vol. 43, no. 1, pp. 1–5, 2016.

[7]. Thibault JB, Sauer KD, Bouman CA, and Hsieh J, "A three-dimensional statistical approach to improved image quality for multislice helical CT," Med. Phys, vol. 34, no. 11, pp. 4526–4544, 2007. [PubMed: 18072519]

[8]. Yu Z, Thibault JB, Bouman CA, Sauer KD, and Hsieh J, "Fast model-based X-ray CT reconstruction using spatially nonhomogeneous ICD optimization," IEEE Trans. Image Process, vol. 20, no. 1, pp. 161–175, 2011. [PubMed: 20643609]

[9]. Othman AE, Brockmann C, Yang Z, Kim C, Afat S, Pjontek R, Nikobashman O, Brockmann MA, Kim JH, and Wiesmann M, "Effects of radiation dose reduction in volume perfusion CT imaging of acute ischemic stroke," Eur. Radiol, vol. 25, col. 12, pp. 3415–3422, 2015. [PubMed: 25903716]

[10]. Murphy A, So A, Lee TY, Symons S, Jakubovic R, Zhang L, and Aviv R, "Low dose CT perfusion in acute ischemic stroke," Neuroradiology, vol. 56, no. 12, pp. 1055–1062, 2014. [PubMed: 25252738]

[11]. Fang R, Zhang S, Chen T, and Sanelli PC, "Robust low-dose CT perfusion deconvolution via tensor total-variation regularization," IEEE Trans. Med. Imag, vol. 34, no. 7, pp. 1533–1548, 2015.

[12]. Zeng D, Zhang X, Bian Z, Huang J, Zhang H, Lu L, Lyu W, Zhang J, Feng Q, Chen W, and Ma J, "Cerebral perfusion computed tomography deconvolution via structure tensor total variation regularization," Med. Phys, vol. 43, no. 5, pp. 2091–2107, 2016. [PubMed: 27147322]

[13]. Mendrik AM, Vonken E, Ginneken BV, Jong HW, Riordan A, Seeters TV, Smit EJ, Viergever MA, and Prokop M, "TIPS bilateral noise reduction in 4D CT perfusion scans produces high-quality cerebral blood flow maps," Phys. Med. Biol, vol. 56, no. 13, pp. 3857–3872, 2011. [PubMed: 21654042]

[14]. Niu S, Zhang S, Huang J, Bian Z, Chen W, Yu G, Liang Z, and Ma J, "Low-dose cerebral perfusion computed tomography image restoration via low-rank and total variation regularizations," Neurocomputing, vol. 197, pp. 143–160, 2016. [PubMed: 27440948]

[15]. Manhart MT, Kowarschik M, Fieselmann A, Zheng YD, Royalty K, Maier AK, and Hornegger J, "Dynamic iterative reconstruction for interventional 4-D C-arm CT perfusion imaging," IEEE Trans. Med. Imag, vol. 32, pp. 1336–1348, 2013.

[16]. Li B, Lyu Q, Ma J, and Wang J, "Iterative reconstruction for CT perfusion with a prior-image induced hybrid nonlocal means regularization: Phantom studies," Med. Phys, vol. 42, no. 6, pp. 3638–3639, 2015.

[17]. Li Y, Speidel MA, Francois CJ, and Chen GH, "Radiation dose reduction in CT myocardial perfusion imaging using SMART-RECON," IEEE Trans. Med. Imag, vol. 36, no. 12, pp. 2557–2568, 2017.

[18]. Zeng D, Xie Q, Cao W, Lin J, Zhang H, Zhang S, Huang J, Bian Z, Meng D, Xu Z, Liang Z, Chen W, and Ma J, "Low-Dose dynamic cerebral perfusion computed tomography reconstruction via Kroneckerbasis-representation tensor sparsity regularization," IEEE Trans. Med. Imag, vol. 36, no. 12, pp. 2546–2556, 2017.

[19]. Geyer LL, Schoepf UJ, Meinel FG, Nance JW, Bastarrika G, Leipsic JA, Paul NS, Rengo M, Laghi A, and Cecco GND,"State of the art: iterative CT reconstruction techniques," Radiology, vol. 276, no. 2, pp. 339357, 2015.

[20]. Chambolle A, "An algorithm for total variation minimization and applications," Kluwer Academic Publishers, pp. 89–97, 2004.

[21]. Beck A and Teboulle M,"Fast gradient-based algorithms for constrained total variation image denoising and deblurring problems," IEEE Trans. Image Process, vol. 18, no. 11, pp. 24192434, 2009.

[22]. Wu H, Maier A, Fahrig R, and Hornegger J, “Spatial-temporal total variation regularization (STTVR) for 4D-CT reconstruction,” in Proceedings of SPIE Medical Imaging, vol. 8313, pp. 83133J, 2012.

[23]. Tian Z, Jia X, Yuan K, Pan T, and Jiang SB, “ Low-dose CT reconstruction via edge-preserving total variation regularization,” Phys. Med. Biol, vol. 56, no. 18, pp. 5949–5967, 2011. [PubMed: 21860076]

[24]. Liu Y, Ma J, Fan Y, and Liang Z, “Adaptive-weighted total variation minimization for sparse data toward low-dose x-ray computed tomography image reconstruction,” Phys. Med. Biol, vol. 57, no. 23, pp. 7923–7956, 2012. [PubMed: 23154621]

[25]. Chen Z, Jin X, Li L, and Wang G, “A limited-angle CT reconstruction method based on anisotropic TV minimization,” Phys. Med. Biol, vol. 58, no. 7, pp. 2119–2141, 2013. [PubMed: 23470430]

[26]. Wang T, Nakamoto K, Zhang H, and Liu H, “Reweighted anisotropic total variation minimization for limited-angle CT reconstruction,” IEEE Trans. Nucl. Sci, vol. 64, no. 10, pp. 2742–2760, 2017.

[27]. Huang Y, Taubmann O, Huang X, Haase V, Lauritsch G, and Maier A, “Scale-space anisotropic total variation for limited angle tomography,” IEEE Trans. Radia. and Plas. Med. Sci, vol. 2, no. 4, pp. 307–314, 2018.

[28]. Wu J, Mou X, Shi Y, Bai T, and Chen Y, “Low-dose computed tomography image reconstruction via structure tensor total variation regularization,” Proceedings of SPIE Medical Imaging, vol. 10573, pp. 105733D, 2018.

[29]. Lefkimmiatis S, Roussos A, Maragos P, and Unser M, “Structure tensor total variation,” SIAM. J. Imaging SCI, vol. 8, no. 2, pp. 1090–1122, 2015.

[30]. Mahmood F, Shahid N, Skoglund U, and Vandergheynst P, “Adaptive graph-based total variation for tomographic reconstructions,” IEEE Signal Proc. Let, vol. 25, no. 5, pp. 700–704, 2018.

[31]. Fang R, Gupta A, Huang J, and Sanelli PC, “TENDER: Tensor non-local deconvolution enabled radiation reduction in CT perfusion,” Neurocomputing, vol. 229, pp. 13–22, 2017. [PubMed: 32523255]

[32]. Li S, Zeng D, Peng J, Bian Z, Zhang H, Xie Q, Wang Y, Liao Y, Zhang S, Huang J, Meng D, Xu Z, and Ma J, “An efficient iterative cerebral perfusion CT reconstruction via low-rank tensor decomposition with spatial-temporal total variation regularization,” IEEE Trans. Med. Imag, vol. 38, no. 2, pp. 360–370, 2019.

[33]. Xie Q, Zhao Q, Meng D, and Xu Z, “Kronecker-Basis-Representation Based Tensor Sparsity and Its Applications to Tensor Recovery,” IEEE Trans. Pattern Anal, vol. 36, no. 12, pp. 2546–2556, 2017.

[34]. Sagheer SVM and George SN, “Denoising of low-dose CT images via low-rank tensor modeling and total variation regularization,” Artif. Intell. Med, vol. 94, pp. 1–17, 2019. [PubMed: 30871676]

[35]. Boyd S, Parikh N, Chu E, Peleato B, and Eckstein J, “Distributed optimization and statistical learning via the alternating direction method of multipliers,” Found. Trends Mach. Learn, vol. 3, no. 1, pp. 1–122, 2011.

[36]. Zhang Y, Zhang D, Li S, Liao Y, Bian Z, Bian Y, He J, Jia X, Xing Y, Meng D, Lu H, and Ma J, “Contrast-medium anisotropy-aware tensor total variation model for robust cerebral perfusion CT reconstruction with weak radiation: a preliminary study,” In Proc. of SPIE (Fully3D 2019), vol. 11072, pp. 110720A, 2019.

[37]. Ma J, Liang Z, Fan Y, Liu Y, Huang J, Chen W, and Lu H, “Variance analysis of x-ray CT sinograms in the presence of electronic noise background,” Med. Phys, vol. 39, no. 7, pp. 4051–4065, 2012. [PubMed: 22830738]

[38]. Natarajan BK, “Sparse approximate solutions to linear systems,” SIAM J. Comput, vol. 24, no. 2, 227–234, 1995.

[39]. Donoho DL, “Compressed sensing,” IEEE Trans. Inform. Theo, vol. 52, no. 4, pp. 1289–1306, 2006.

[40]. Elbakri IA and Fessler JA, “Statistical image reconstruction for polyenergetic X-ray computed tomography,” IEEE Trans. Med. Imag, vol. 21, no. 2, pp. 89–99, 2002.

[41]. Nien H and Fessler JA, “Relaxed linearized algorithms for faster Xray CT image reconstruction,” IEEE Trans. Med. Imag, vol. 35, no. 4, pp. 1090–1098, 2016.

[42]. Wang Z, Bovik AC, Sheikh HR, and Simoncelli EP, “Image quality assessment: from error visibility to structural similarity,” IEEE Trans. Image. Process, vol. 13, no. 4, pp. 600–612, 2004. [PubMed: 15376593]

[43]. Zhang Y, Mou X, Wang G, and Yu H, “Tensor-based dictionary learning for spectral CT reconstruction,” IEEE Trans.Med. Imag, vol. 36, no. 14, pp. 142–154, 2016.

[44]. Hu Z, Gao J, Zhang N, Yang Y, Liu X, Zheng H, and Liang D, “An improved statistical iterative algorithm for sparse-view and limited-angle CT image reconstruction,” Scientific Reports, vol. 7, no. 1, pp. 10747, 2017. [PubMed: 28878293]

[45]. Gong C, Han C, Gan G, Deng Z, Zhou Y, Zhou Y, Yi J, Zeng X, Xie C, and Jin X, “Low-dose dynamic myocardial perfusion CT image reconstruction using pre-contrast normal-dose CT scan induced structure tensor total variation regularization,” Phys. Med. Biol, vol. 62, no. 7, pp. 2612–2635, 2017. [PubMed: 28140366]

[46]. Yin X, Zhao Q, Liu J, Yang W, Yang J, Quan G, Chen Y, Shu H, Luo L, and Coatrieux J, “Domain progressive 3D residual convolution network to improve low-dose CT imaging,” IEEE Trans.Med. Imag, vol. 38, no. 12, pp. 2903–2913, 2019.

[47]. Kingma DP and Ba JL, “Adam: A method for stochastic optimization,” In Proc. ICLR 2015 Conf, pp. 1–15, 2015.

[48]. Fieselmann A, Kowarschik M, Ganguly A, Hornegger J, and Fahrig R, “Deconvolution-based CT and MR brain perfusion measurement: Theoretical model revisited and practical implementation details,” International Journal of Biomedical Imaging, vol. 2011, pp. 467563, 2011. [PubMed: 21904538]

[49]. Frosio I and Kautz J, “Statistical nearest neighbors for image denoising,” IEEE Trans. Image. Process, vol. 28, no. 2, pp. 723–738, 2019. [PubMed: 30222562]

[50]. Hirata M, Sugawara Y, Murase K, Miki H, and Mochizuki T, “Evaluationof optimal scan duration and end time in cerebral CT perfusion study,” Radiat. Med, vol. 23, no. 5, pp. 351–363, 2005. [PubMed: 16342908]

[51]. Abels B, Klotz E, Tomandl BF, Villablanca JP, Kloska SP, and Lell MM, “CT perfusion in acute ischemic stroke: a comparison of 2-second and 1-second temporal resolution,” AJNR Am. J. Neuroradiol, vol. 32, no. 9, pp. 1632–1639, 2011. [PubMed: 21816919]

[52]. Zeng D, Gong C, Bian Z, Huang J, Zhang X, Zhang H, Lu L, Niu S, Zhang Z, Liang Z, Feng Q, Chen W, and Ma J, “Robust dynamic myocardial perfusion CT deconvolution for accurate residue function estimation via adaptive-weighted tensor total variation regularization: a preclinical study,” Phys. Med. Biol, vol. 61, no. 22, pp. 8135–8156, 2017.

[53]. Yao L, Zeng D, Chen G, Liao Y, Li S, Zhang Y, Wang Y, Tao X, Niu S, Lv Q, Bian Z, Ma J, and Huang J, “Multi-energy computed tomography reconstruction using a nonlocal spectral similarity model,” Phys. Med. Biol, vol. 64, no. 3, pp. 035018, 2019. [PubMed: 30577033]

[54]. Chen S, Liu H, Hu Z, Zhang H, Shi P, and Chen Y, “Simultaneous reconstruction and segmentation of dynamic PET via low-rank and sparse matrix decomposition,” IEEE Trans. Biomed. Eng, vol. 62, no. 7, pp.1784–1795, 2015. [PubMed: 25706502]

[55]. Trémoulhéac B, Dikaios N, Atkinson D, and Arridge SR, “Dynamic MR image reconstruction-separation from undersampled (k, t)-space via low-rank plus sparse prior,” IEEE Trans. Med. Imag, vol. 33, no. 8, pp.1689–1701, 2014.

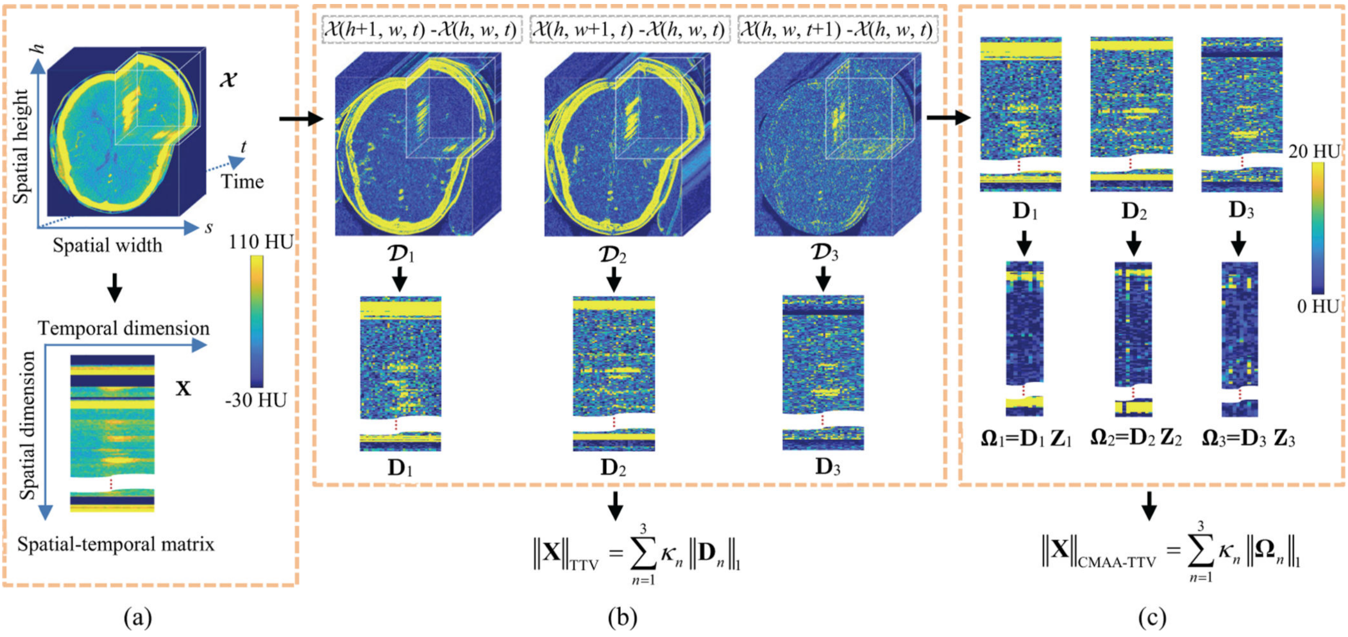

Fig. 1.

Illustration of the TTV and proposed CMAA-TTV model. (a) Illustration of the 3D tensor representation $\mathscr{X} \in \mathbb{R}^{N_h \times N_w \times N_t}$ (upper) and the 2D spatial-temporal matrix representation $\mathbf{X} \in \mathbb{R}^{(N_h N_w) \times N_t}$ (lower) of a real PCT object. (b) Illustration of the TTV model. The upper figures represent the difference tensors of $\mathscr{X}$ in the spatial height, weight and temporal domains, respectively, and the lower figures represent the corresponding 2D spatial-temporal forms. (c) Illustration of the proposed CMAA-TTV model. The lower figures represent the subspace basis matrices $\mathbf{\Omega}_n \in \mathbb{R}^{(N_h N_w) \times r}$ calculated implicitly on the $\mathbf{D}_n$.

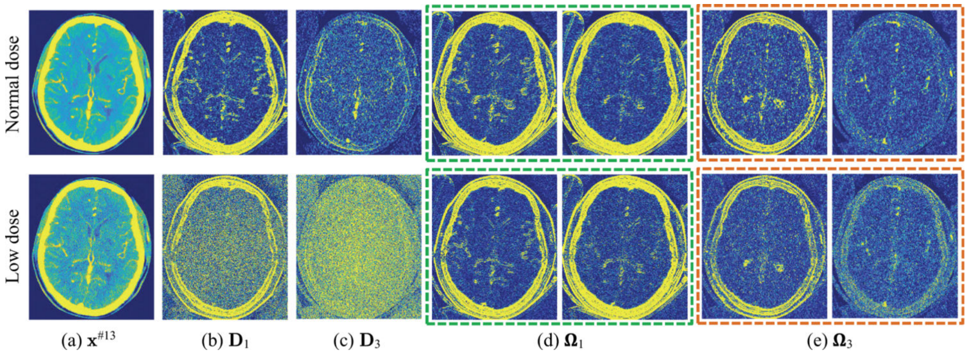

Fig. 2.

Illustration of the difference between the directly calculated difference matrix $\mathbf{D}_n$ and the implicitly calculated basis matrix Ω_n (the rank r was set as 13). (a) One frame (#13) of the normal-dose reference PCT (upper) and the low-dose simulations (lower). (b)-(c) Corresponding difference matrices of frames in (a), where $\mathbf{D}_1$ and $\mathbf{D}_3$ are obtained by directly calculating along the spatial height and temporal dimensions, respectively. (d) Illustration of two typical column vectors (reshaped to be the size of $N_h \times N_w$ for visual observation) in the basis matrix Ω_1 calculated upon $\mathbf{D}_1$. (e) Illustration of the two typical column vectors in the basis matrix Ω_3 calculated upon $\mathbf{D}_3$.

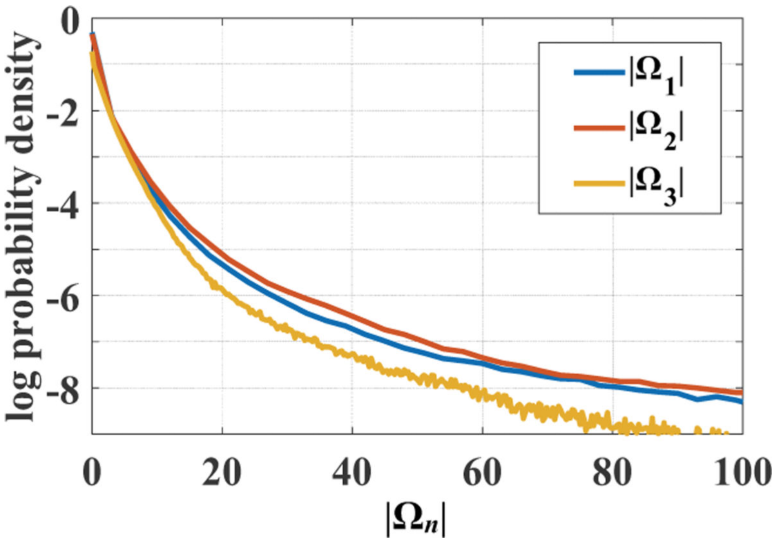

Fig. 3.

Distribution of absolute values in the basis matrix.

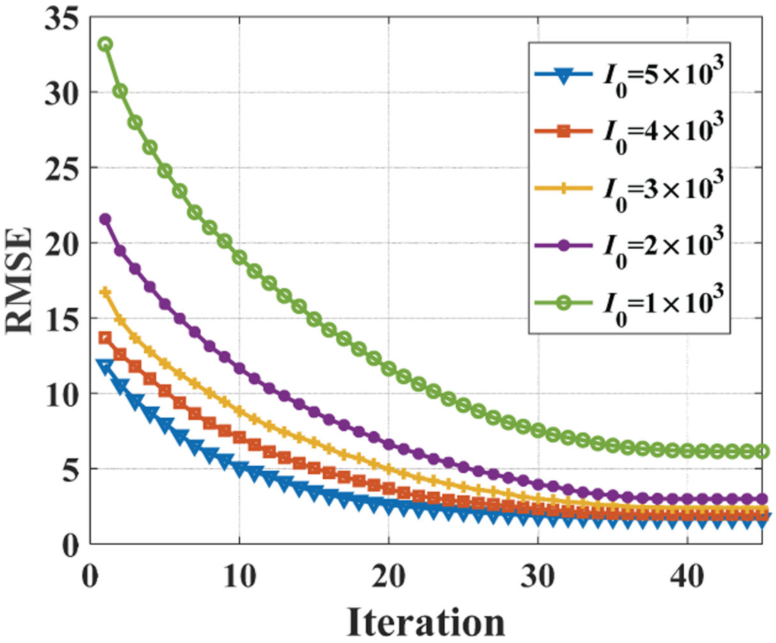

Fig. 4.

Convergence behaviour of the proposed CMAA-TTV algorithm.

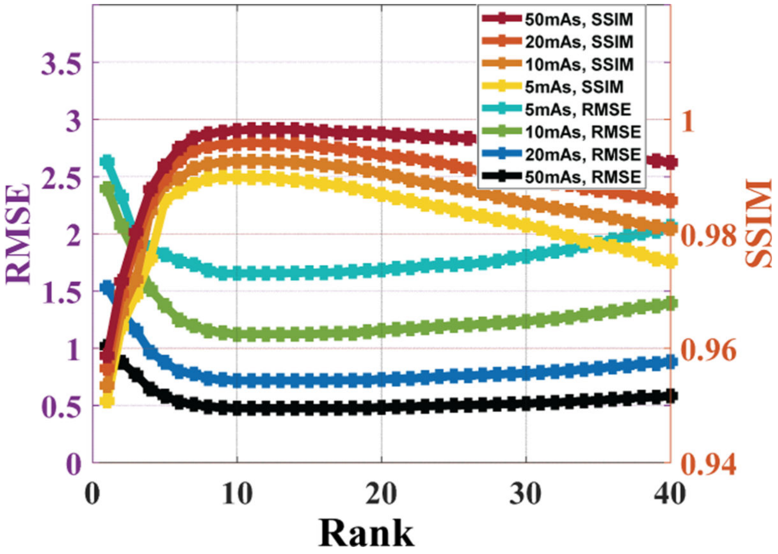

Fig. 5.

RMSE and SSIM values of the results reconstructed by the CMAA-TTV algorithm for the digital brain perfusion phantom with different rank versus different simulated radiation levels.

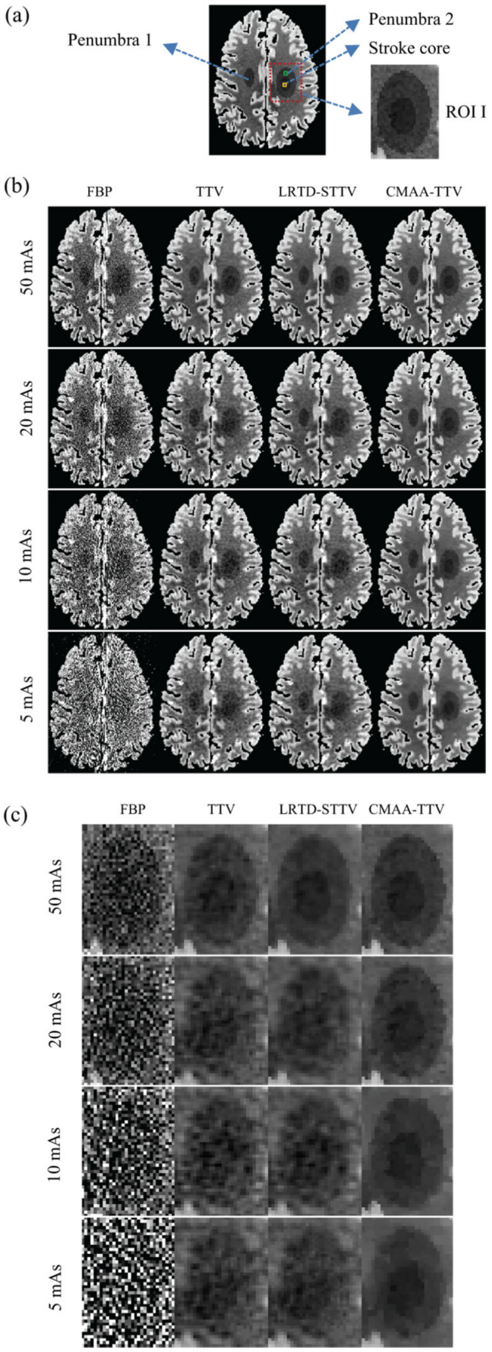

Fig. 6.

Illustration of (a) one frame (#17) of the digital brain perfusion phantom, (b) the corresponding reconstructed results at various simulated tube current-time product levels, and (c) the zoomed images of ROI 1. From top to bottom of (b) and (c) show low-dose simulations at 50, 20, 10 and 5 mAs, respectively, and from left to right of (b) and (c) show reconstructed results using the FBP, TTV, LRTD-STTV and CMAA-TTV algorithms, respectively. The display window is [20, 60].

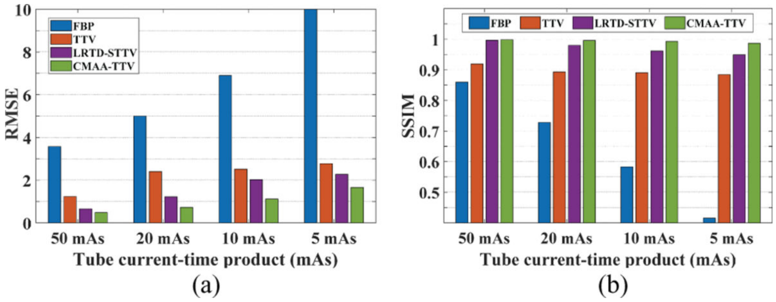

Fig. 7.

Performance comparison of different algorithms based on (a) RMSE and (b) SSIM metrics.

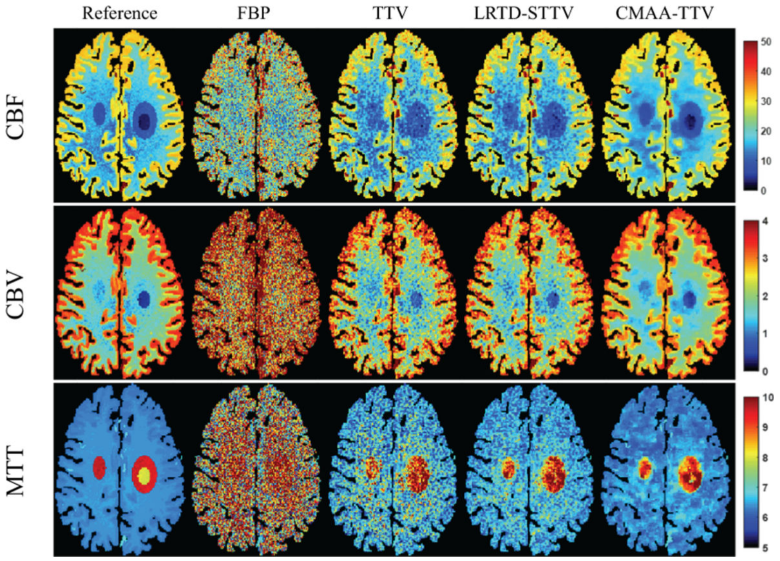

Fig. 8.
CBF, CBV and MTT maps from the reference phantom and reconstructed results obtained by different algorithms at a tube current-time product level of 5 mAs. The units for the CBF, CBV and MTT are ml/100g/min, ml/100g and s (second), respectively.

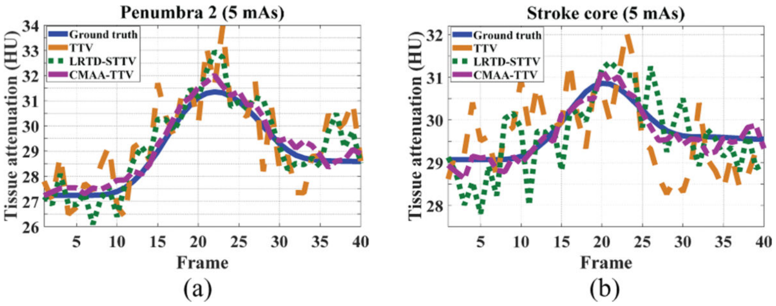

Fig. 9.

Comparison of TDC curves obtained with different methods for two ROIs of the digital brain phantom at a tube current-time product level of 5 mAs. Panel (a) shows the results for the right penumbra and panel (b) shows the results for the stroke core.

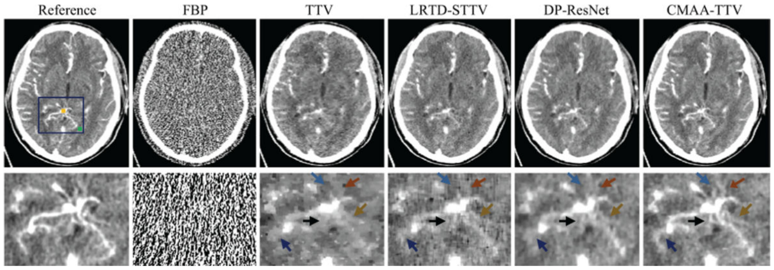

Fig. 10.

Reconstructed results from simulated patient data (patient #S1) at frame 12. From left to right: the reference image and the reconstructed results from simulated low-dose data by the FBP, TTV, LRTD-STTV, DP-ResNet and CMAA-TTV algorithms, respectively. The lower row shows zoomed images of a selected region (as marked by the blue rectangle). The display window is [−20, 120] HU. Please zoom in the figure for more details.

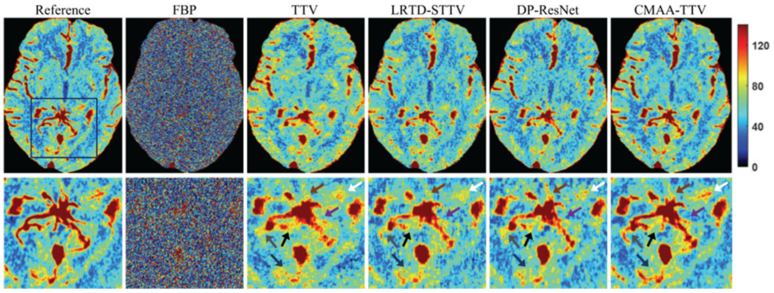

Fig. 11.

CBF maps from the reconstructed results of patient #S1. From left to right: CBF maps calculated from the reference data and reconstructed results from simulated data by the FBP, TTV, LRTD-STTV, DP-ResNet and CMAA-TTV algorithms, respectively. The lower row shows zoomed images of a selected region (as marked by the blue rectangle). The unit is ml/100g/min. Please zoom in the figure for more details.

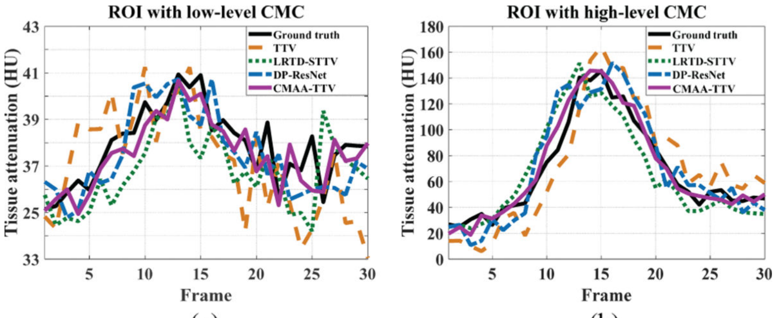

(a) (b)

Fig. 12.

Comparison of TDC curves obtained with different methods for two ROIs in the simulated patient data: (a) an ROI with relatively low CMC; and (b) an ROI with relatively high CMC.

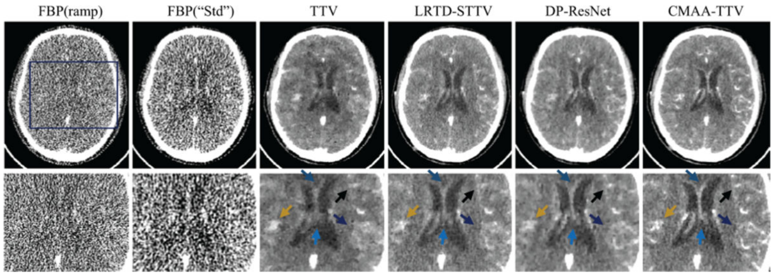

Fig. 13.

Reconstructed results from frame 15 of real clinical PCT data obtained at 80 kVp/20 mAs (patient #C1). From left to right: reconstructed results obtained using FBP with the ramp filter, FBP with the commercial kernel "Std", TTV, LRTD-STTV, DP-ResNet and the proposed CMAA-TTV algorithm, respectively. The lower row shows zoomed images of a selected region (as marked by the blue rectangle). The display window is [−20, 120] HU. Please zoom in the figure for more details.

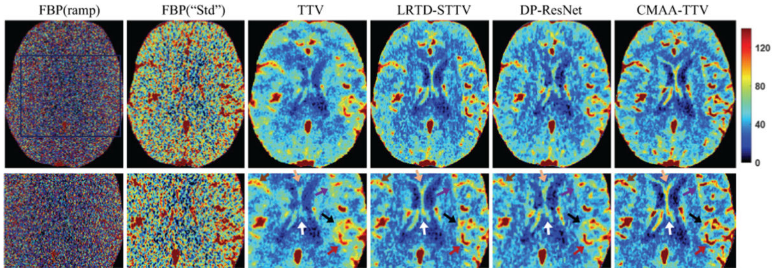

Fig. 14.

CBF maps from the reconstructed results from patient #C1. From left to right: CBF maps calculated from the reconstructed results obtained using FBP with the ramp filter, FBP with the commercial kernel "Std", TTV, LRTD-STTV, DP-ResNet and the proposed CMAA-TTV algorithm, respectively. The lower row shows zoomed images of a selected region (as marked by the blue rectangle). The unit is ml/100g/min. Please zoom in the figure for more details.

TABLE I:

RMSE and SSIM accuracies of the hemodynamic parameter maps from the digital phantom.

		RMSE				SSIM			
		FBP	**TTV**	**LRTD-STTV**	**CMAA-TTV**	**FBP**	**TTV**	**LRTD-STTV**	**CMAA-TTV**
50 mAs	CBF	5.0775	1.9305	0.9568	**0.7945**	0.9678	0.9939	0.9981	**0.9986**
	CBV	0.6108	0.2232	0.1225	**0.0987**	0.9629	0.9952	0.9984	**0.9989**
	MTT	1.0779	0.1639	0.1014	**0.0547**	0.9515	0.9928	0.9977	**0.9980**
20 mAs	CBF	5.9642	3.9701	2.8186	**1.0966**	0.9385	0.9837	0.9935	**0.9982**
	CBV	0.7489	0.3960	0.2401	**0.1498**	0.9389	0.9845	0.9919	**0.9983**
	MTT	1.6371	0.3945	0.2993	**0.1679**	0.9203	0.9728	0.9811	**0.9975**
10 mAs	CBF	7.2422	4.5460	3.7648	**2.1495**	0.8582	0.9796	0.9826	**0.9922**
	CBV	0.9841	0.4530	0.3405	**0.2547**	0.8604	0.9801	0.9839	**0.9927**
	MTT	2.1307	0.4976	0.3378	**0.2549**	0.8458	0.9626	0.9753	**0.9885**
5 mAs	CBF	9.7236	6.1306	4.6078	**2.9886**	0.7915	0.9701	0.9759	**0.9894**
	CBV	1.4622	0.5953	0.4979	**0.3094**	0.7836	0.9684	0.9755	**0.9903**
	MTT	2.5743	0.7205	0.4721	**0.2853**	0.7591	0.9497	0.9661	**0.9808**

TABLE II:

RMSE and SSIM accuracies (mean ±SDs) of the hemodynamic parameter maps from the simulated low-dose patient data.

			RMSE		
	FBP	**TTV**	**LRTD-STTV**	**DP-ResNet**	**CMAA-TTV**
CBF	67.284±5.362	18.768±3.538	14.908±2.921	13.128±3.284	**8.790±1.672** [*]
CBV	12.064±2.073	3.339±0.969	2.676±0.862	2.731±0.790	**1.891±0.466** [*]
MTT	3.490±0.933	0.674±0.124	0.484±0.085	0.519±0.069	**0.276±0.043** [*]
			SSIM		
	FBP	**TTV**	**LRTD-STTV**	**DP-ResNet**	**CMAA-TTV**
CBF	0.4169±0.093	0.8463±0.028	0.8672±0.021	0.9017±0.019	**0.9326±0.009** [*]
CBV	0.4263±0.091	0.8528±0.046	0.8719±0.032	0.8836±0.039	**0.9341±0.011** [*]
MTT	0.3829±0.122	0.8075±0.063	0.8734±0.055	0.8593±0.041	**0.9287±0.024** [*]

[*] Significantly different from the SSIM scores for other algorithms (P<0.05).

TABLE III:

Radiologists' scoring (mean ±SDs) of the hemodynamic parameter maps for different algorithms from the patient data.

Radiologists	FBP	TTV	LRTD-STTV	DP-ResNet	CMAA-TTV
Radiologist #1	1.96±0.21	2.99±0.50	3.48±0.38	3.45±0.44	**4.12±0.24** *
Radiologist #2	1.53±0.28	2.73±0.57	3.20±0.45	3.22±0.53	**4.04±0.31** *
Radiologist #3	2.07±0.24	3.11±0.46	3.54±0.41	3.51±0.39	**4.16±0.22** *

* Significantly different from the scores for other algorithms (P<0.05).